ORIGINAL ARTICLE

Experimental and Numerical Analysis of a Motorcycle Air Intake System Aerodynamics and Performance

M. A. Abd Halim, N. A. R. Nik Mohd*, M. N. Mohd Nasir and M. N. Dahalan

Aeronautics Laboratory, School of Mechanical Engineering, Faculty of Engineering, Universiti Teknologi Malaysia, 81310 Skudai Johor, Malaysia

ABSTRACT – Induction system or also known as the breathing system is a sub-component of the internal combustion system that supplies clean air for the combustion process. A good design of the induction system would be able to supply the air with adequate pressure, temperature and density for the combustion process to optimizing the engine performance. The induction system has an internal flow problem with a geometry that has rapid expansion or diverging and converging sections that may lead to sudden acceleration and deceleration of flow, flow separation and cause excessive turbulent fluctuation in the system. The aerodynamic performance of these induction systems influences the pressure drop effect and thus the engine performance. Therefore, in this work, the aerodynamics of motorcycle induction systems is to be investigated for a range of Cubic Feet per Minute (CFM). A three-dimensional simulation of the flow inside a generic 4-stroke motorcycle airbox were done using Reynolds-Averaged Navier Stokes (RANS) Computational Fluid Dynamics (CFD) solver in ANSYS Fluent version 11. The simulation results are validated by an experimental study performed using a flow bench. The study shows that the difference of the validation is 1.54% in average at the total pressure outlet. A potential improvement to the system have been observed and can be done to suit motorsports applications.

INTRODUCTION

The airbox of an engine is a plenum of air from which the engine cylinders draw from. Modern engines draw air from the atmosphere into an airbox, which is connected by individual hoses to each carburettor or directly to the intake ports in fuel-injected engines [1]. This air is, in turn, replenished from the atmosphere through the restrictor, throttle body and intake trumpet. A complete understanding of the flow dynamics of an airbox is important since the primary function of an air intake system is to supply the engine with the correct amount of clean air [2] with the correct amount for the required combustion process. The piston moves downward increasing the volume of the combustion chamber and allowing air and fuel to be pulled in during the intake stroke of the piston and reaches bottom dead centre [3]. The flow efficiency of the intake system has a direct impact on te power that the engine is able to deliver [4-7]. In a study related to AIS by Makgata [8], it is expected that an increase of 6.2% to the engine power can be gained from an improved airbox that inducts 6.2% more airflow. The speed of air generated by the intake system can be a significant contributor to the unsteady nature of separated flow that affects the manifold on charging and discharging. A properly designed airbox is crucial for the inlet manifold to enable the engine to ingest air [2, 9]. Thus the inside diameter of the manifold must be able to accommodate the bulk airflow to avoid low volumetric efficiency. It may be noted that since the pressure loss from the intake duct towards the atmosphere, the atmospheric pressure or environmental pressure where the air is sucked in is assumed to be the inlet [10] and the outlet is further attached to inlet manifold.

The airbox may be divided into three main parts: an inlet pipe and an intake section in which the incoming "dirty" air is guided into, a filter-box section where a filter is located that cleans the polluted air and hinders soot and other particles from entering the cylinders, and an outlet which is the inlet to the intake manifold of the engine. The inlet pipe is usually bent or S-shaped. The flow in such as diffusing S-ducts is complex due to effects arising from the offset between the intake plane and engine face plane. As the flow moves on through the duct, it would be expected that a similar motion in the opposite sense is initiated at the second bend. However, at this stage of the low energy flow is largely on the outside wall relative to the second bend of the tube and is not driven back circumferentially [11] which causes strong pressure-driven stream-wise vortices [12]. The outlet pipe could be varied for optimisation. A common practice used in motorsport is adding a velocity stack to the outlet pipe [13] for extra power motorcycle engines. Generally, when a velocity stack is used on an engine, an air filter is not used. To minimise flow resistance, the outlet pipe, which is the inlet to the intake manifold should have no sharp bends and the interior wall surface should be smooth [14]. Giannakopoulos, Frouzakis [15] studied the incompressible flow in the intake pipe of an internal combustion engine. It was found that the flow can become turbulent very quickly depending on the inflow profile imposed at the pipe inlet, even though no additional noise was added to mimic turbulent velocity fluctuations.

Numerous experimental papers [16-18] have been carried out. They show that the enrichment of oxygen in the intake air would help in better combustion and result in higher heat release for the same quantity of fuel. Reynolds Averaged

Navier-Stokes (RANS) approach has been used to study the flow in air intake systems, predicting the formation of separated flow regions depending on the RPM, engine displacements and Reynolds number. Yerram, Prasad [19]; Ramasamy, Zamri [20]; HoseopSong and Cho [21] investigated the design optimisation of air intake system by adding guide vane using the κ-ε model, revealing improved overall pressure drop by 22% and 12.01% respectively. It was reported that the κ-ε model in a steady-state shows reasonably good agreement for the intake system cases [14, 22, 23].

Furthermore, Phulpagar and Gohel [23] stated that CFD result shows 9-10% of the variation in results compared to experimental tests. Patankar, Pratap [24] adopted a κ-ε type turbulence model to numerically predict the flow development in a curved pipe, recognising that the numerical prediction capability was not as satisfactory as for laminar flows. Lee, Allan [12] and Halim, Mohd [25] investigated a numerical analysis of the airflow inside an S-shaped tube using three different turbulence models, namely the κ-ε baseline κ-ω and κ-ω with Transport of Shear Stress (SST) models at the steady-state condition. The SST model has performed much better than the other two turbulence models. The latter approximately capturing the qualitative trends but failing to predict the actual magnitudes of the calculated flow features. Sedlacek and Skovajsa [26] optimises the basic shape of the airbox using the κ-ω SST turbulence model in a transient state to find the most appropriate design.

This paper discusses explicitly the flow characteristics of air flowing inside a generic 4-stroke motorcycle airbox. The direction of the flow is from the atmospheric to the outlet clean pipe connected to the throttle body. A numerical investigation of the flow in the standard airbox was conducted using the ANSYS Fluent κ-ω SST turbulence model. The CFD simulation results were validated using a commercial flow bench. The characteristic flow features upon volume in Cubic Feet per Minutes (CFM) changes and the total pressure of air entering the throttle body are the parameters of interest.

EXPERIMENTAL SETUP

The airbox was meant to serve a single-cylinder 4-stroke spark ignition engine motorcycle. The engine's displacement was 150 cc with a bore and stroke of 57 mm and 58.7 mm respectively. In the present work, the airbox was tested without an air filter. Resonant was blocked to prevent pressure loss. Figure 1a shows the blockage of the resonant using a custom-made jig tool and clay.

The flow bench equipment, SuperFlow SF-750, was used to measure the characteristics of air entering the airbox. The flow bench consisted of an open circuit ducting system that had an air pump at the downstream to induce airflow. The pressure within the ducting system could be varied by changing the speed of the air pump. The eye of the blower was connected to the exit of the airbox using a jig to simulate the actual working condition of the airbox attached to the throttle body. Figure 1(a) to 1(c) show the components of the experimental setup. Experiments were carried out with different volumetric airflow rates (CFM) sucked through the airbox by adjusting the blower speed. The specifications of the flow bench system are shown in Table 1.
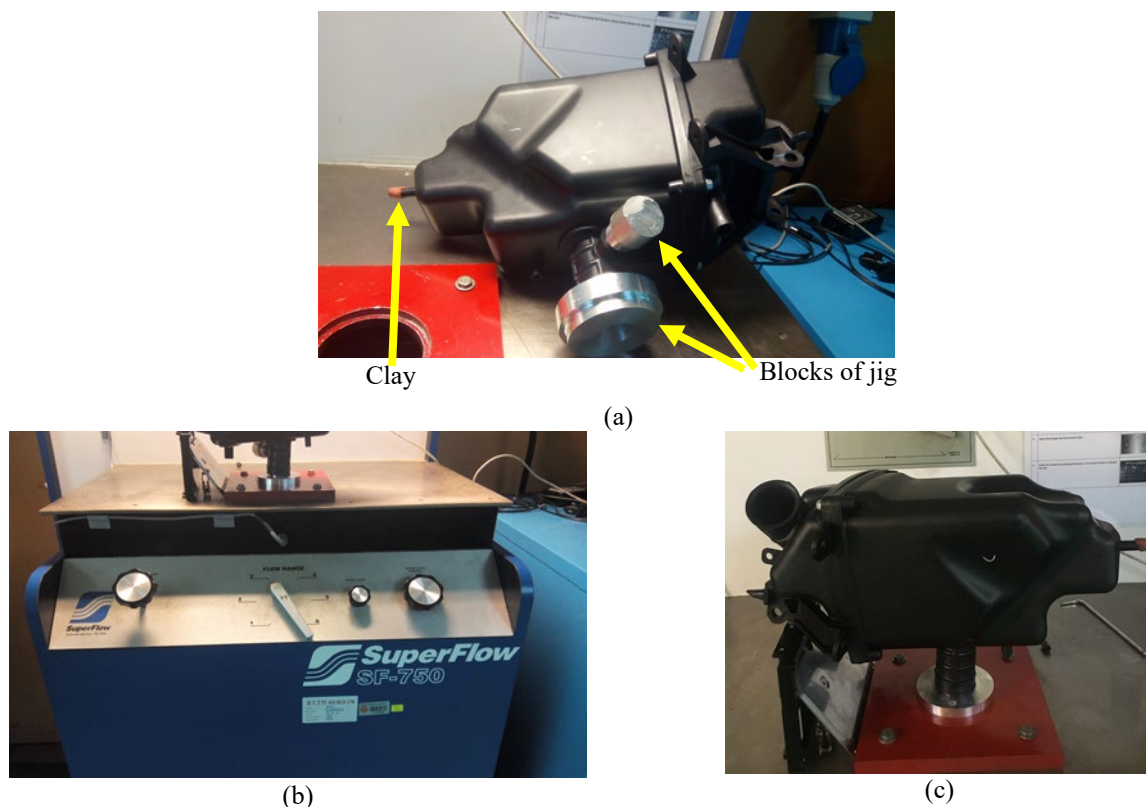

Clay   Blocks of jig

(a)

(b)

(c)

Figure 1. Settings of the flow bench test.

To ensure that the experiment was well preserved and the result was in a consistence range, the room temperature was at a constant range. The fluid properties conditions such as the air density, $\rho = 1.1835$ kg/m^3, atmospheric pressure which is 0.996 atm and relative humidity is 62%. Before the testing was conducted, a calibration test on the flow bench has been done based on the jig block. For setting up the calibration test, a calibration plate was placed onto the orifice of the suction section of the flow bench and was tested without the airbox. The calibration process was tested to reach a specific high CFM value for at least three times. Other properties such as temperature and total pressure at the outlet were taken at least three times for every set of CFM, and the average value were considered.

Table 1. Specifications of the flow bench system.

Parameter	Values
Calibration test pressure	25" of water
Range	0-750 cfm
Capacity	660 cfm @ 25" of water
Power	240 VAC, 40A single phase
Weight	400 lbs (181 kg)
Dimensions	35 x 27 x 80 in. (89 x 69 x 204 cm)

From the experiment test using the flow bench, the temperature and pressure at the outlet were taken three times. The average values was considered throughout the analysis for CFD calculation. Mass flow rate was calculated based on the average value of temperature and gained pressure outlet. Tables 2 – 3 shows the results obtained from the flow bench test. The tests were conducted on the same day, where the temperature was around 26 °C (Table 2).

Table 2. Temperature reading taken at the outlet

CFM	Temperature reading 1 (°C)	Temperature reading 2 (°C)	Temperature reading 3 (°C)	Average temperature (°C)
50	26.04	26.07	26.02	26.04
70	26.09	26.09	25.84	26.01
90	26.04	25.93	25.82	25.93
110	25.91	25.68	25.61	25.73
130	25.72	25.54	25.41	25.56

Table 3. Pressure and mass flow rate reading taken at the outlet

CFM	Total pressure outlet 1 (in H$_2$O)	Total pressure outlet 2 (in H$_2$O)	Total pressure outlet 3 (in H$_2$O)	Average total pressure outlet (Pa)	Mass flow rate (kg/s)
50	-7.06	-7.08	-7.04	-1757	0.027
70	-12.8	-12.8	-12.8	-3186	0.038
90	-20.1	-20.1	-20.1	-5004	0.049
110	-30.5	-30.5	-30.5	-7593	0.060
130	-41.5	-41.7	-41.6	-10356	0.0720

GEOMETRICAL PARAMETERS

Governing Equations

For numerical analysis, the geometry of the airbox was remodelled and presented in Figure 2a and Figure 2b. The airbox consists of an asymmetrical inlet S-shaped duct, an airbox chamber without filter and an outlet pipe. The model design would resemble the path of air from atmosphere outside the airbox entering the throttle body. The inlet and outlet diameter are 38.45 *mm* and 28.2 *mm*, respectively.

NUMERICAL SETUP

Governing Equations

A commercially available CFD solver, ANSYS Fluent 11 has been used throughout this work. The governing equations [26] for the mean flow in reduced form for steady incompressible flows is given below:

$$\frac{\partial \rho}{\partial t} + \frac{\partial}{\partial x_i}(\rho u_i) = 0 \tag{1}$$

$$\frac{\partial}{\partial t}(\rho u_i) + \frac{\partial}{\partial x_j}(\rho u_i u_j) = -\frac{\partial \rho}{\partial x_i} + \frac{\partial}{\partial x_j}\left[\mu_{eff}\left(\frac{\partial u_i}{\partial x_j} + \frac{\partial u_j}{\partial x_j} - \frac{2}{3}\delta_{ij}\frac{\partial u_l}{\partial x_l}\right)\right] + \frac{\partial}{\partial x_j}(-\rho\overline{u'_i u'_j}) \qquad (2)$$

where u is the velocity vector written in Einstein notation, ρ is the fluid density. These equations have the same general form as the instantaneous Navier-Stokes equations, with the velocities and other solution variables representing the time-averaged values. Additional terms in Equation 2 represents the effects of turbulence. These Reynolds stresses $-\rho\overline{u'_i u'_j}$ must be modelled in order to close the momentum equation.

(a)   (b)
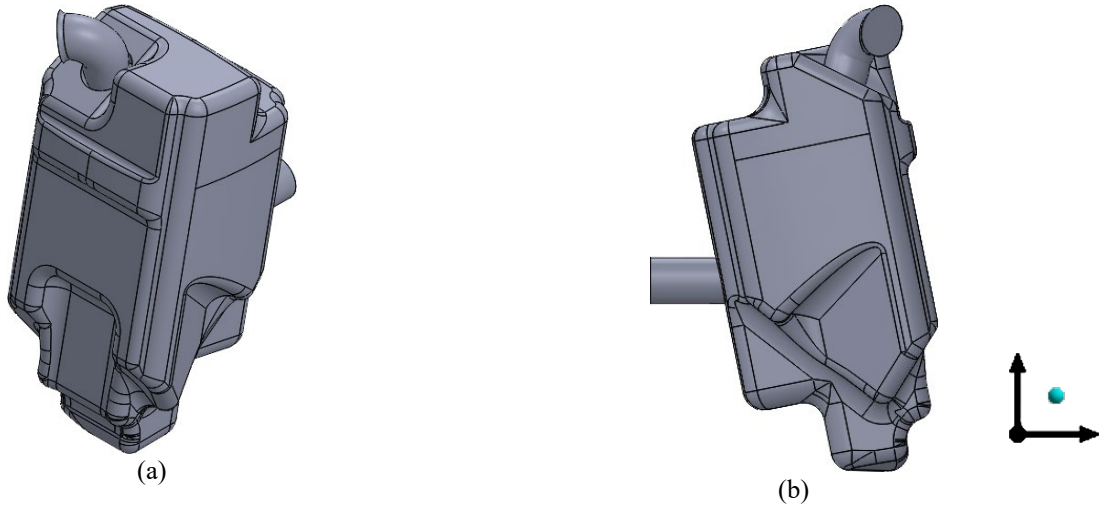
Figure 2. The basic inner volume of airbox viewed from (a) isometric; (b) side.

In this work, the κ-ω model with shear stress transport (SST) [27, 28] is chosen due to its adequate accuracy in modelling turbulent flows at a reliable cost over the higher-order turbulence models. The turbulence closure considered is:

$$\frac{\partial}{\partial t}(\rho k) + \frac{\partial}{\partial x_j}(\rho k u_j) = \frac{\partial}{\partial x_j}\left[(\mu + \sigma_k \mu_t)\frac{\partial k}{\partial x_j}\right] + \rho P - \beta^* \rho \omega k \qquad (3)$$

$$\frac{\partial}{\partial t}(\rho\omega) + \frac{\partial}{\partial x_j}(\rho\omega u_j) = \frac{\partial}{\partial x_j}\left[(\mu + \sigma_\omega \mu_t)\frac{\partial \omega}{\partial x_j}\right] + \frac{\gamma}{\nu_t}P - \beta\rho\omega^2 + 2(1 - F_1)\frac{\rho\sigma_{\omega2}}{\omega}\frac{\partial k}{\partial x_j}\frac{\partial \omega}{\partial x_j} \qquad (4)$$

Unsteady terms in Eq. (3) and Eq. (4) are dropped due to the steady-state condition. The term F_1 for the k-ε model is neglected as it goes near the wall surface whilst for the k-ω model converts to one is it goes near the boundary layer. The model is a combination of the κ-ω turbulence model and κ-ε turbulence model such that the κ-ω plays a role in the inner region of the boundary layer and it switches to the κ-ε in the far from the wall surface flow. The calculation of the distance from the wall is obtained by the solution of a Poisson equation.

The pressure-velocity correlation coupled between velocity and pressure using Semi-Implicit Method for Pressure Linked Equation (SIMPLE) [29]. Spatial discretisation was performed with least squares cell based gradients and second-order accurate scheme of pressure. To reduce the discontinuity, oscillation and spurious in the prediction of momentum, turbulent kinetic energy and specific dissipation rate in the region with a high gradient, the third-order accurate Monotonic Upwind Scheme for Conservative scheme of Laws (MUSCL) by Van Leer [30] was used. The assumption of anisotropic turbulence field used in this turbulence model applied to the current application.

Discretisation of Elements

The physical geometry of the airbox was discretised with tetrahedron dominated elements (Figure 3). To treat the flow in the viscous sub layer region accurately, the mesh in the boundary layer constructed with 9 layers of hexahedral elements with the $y^+ \leq 1$ ($\Delta y = 9.388 \times 10^{-4}\,m$). y^+ is defined as the wall distance non-dimensionalised by the friction and determined based on flat plate theory. A factor of 2 was calculated to the first cell height due to Fluent's cell centred code. Thus, $\Delta y = 1.878 \times 10^{-5}\,m$. Mesh expansion in the boundary layer is developed to follow an exponential distribution as shown in Figure 4.
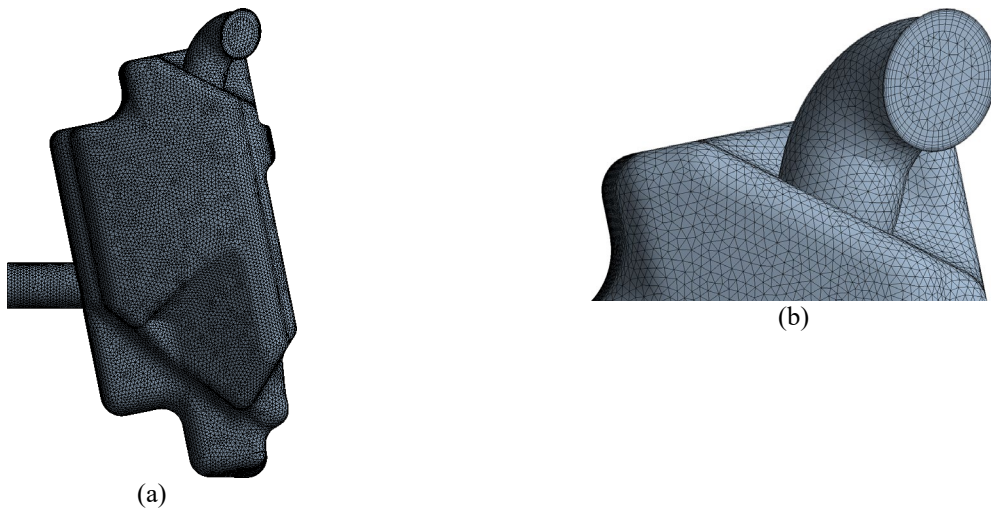
(a)

(b)

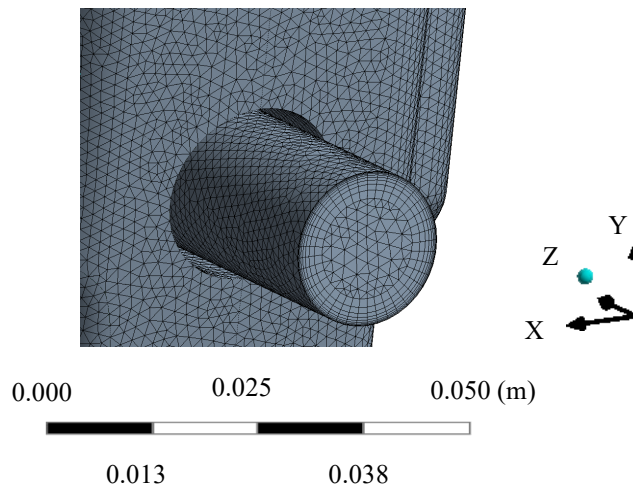**Figure 3.** Global mesh topology of the airbox.

Figure 4. Views of the inflation layer at the outlet pipe with $y^+ \leq 1$.

Mesh Independence Study

A mesh independence study was performed to provide a solution that is independent of mesh, at least for accurately capturing the pressure and velocity distribution inside the airbox [31]. Considering the volume airflow rate at 18 cfm, the changes in the total pressure due to the change in the mesh resolution taken at the outlet is shown in Figure 5. The mesh independence study shows that the percentage difference between 0.65 million and 3 million mesh elements is at 4.2%. Compared, the highest number of elements with 2 million elements is 1.22%. Thus, mesh with 2.0 million elements is considered throughout this work.
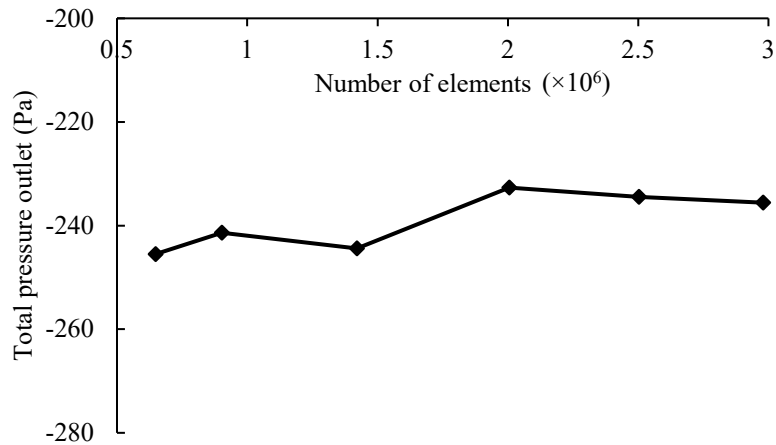

Figure 5. Mesh independence study of generic Y15ZR airbox simulation.

Boundary Conditions

CFD domain and the boundary conditions used are shown in Figure 6. For the upstream boundary condition, pressure-inlet boundary condition was used and set at atmospheric pressure condition. Whereas the downstream boundary of the duct, the mass flow-outlet was used and it varies with CFMs of 50, 70, 90, 110 and 130. At normal temperature and pressure conditions, the air was used as fluid media, which was assumed to be steady and incompressible. The near-wall cell thickness was calculated to satisfy the logarithmic law of the wall boundary. Other fluid properties were taken as constants where, the air density, $\rho = 1.1835$ kg/m^3 and dynamic viscosity, $\mu = 1.835$ x 10^{-5} kg/m^{-s}. Relative humidity was 62% to validate with the experiment condition. Table 3 shows the summary of the CFD parameters and its values.
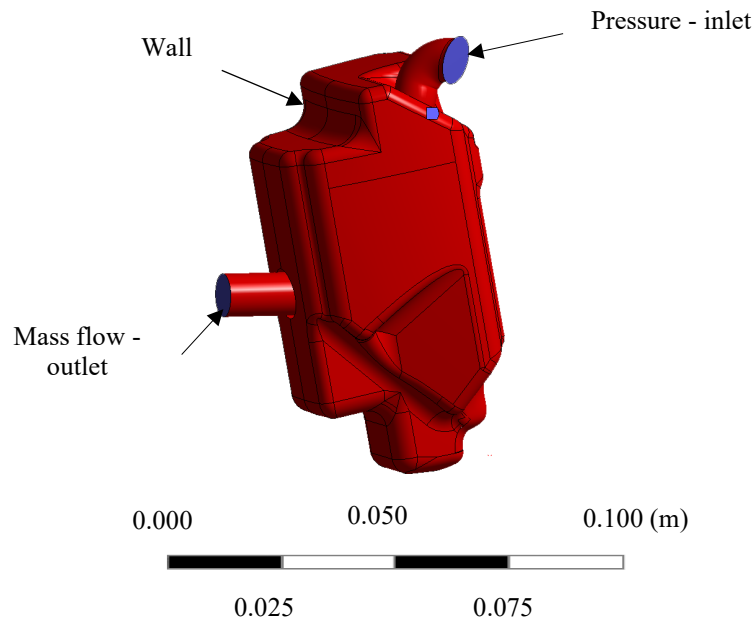

Figure 6. Boundary conditions for CFD

Table 3. Summary of CFD solver set up

Parameters	Values
CFM	50, 70, 90, 110 and 130
Inlet turbulence intensity of	5%
Solution method	Steady state
Solution algorithm	SIMPLE
Turbulence model	κ-ω SST model
Maximum residual tolerance	0.0001
Resolution scheme	Third-order MUSCL
y^+ value	1

RESULTS AND DISCUSSION

Validation of κ-ω SST Model with Experimental Data

CFD analysis was carried out with different mass flow rates based on CFM. From CFD, the calculated total pressure at the outlet decreases across the intake system and increases as the airbox CFM increases. For comparison, the measurement of the total pressure of air intake system was conducted with the same load condition. The comparison of the total pressure at the outlet is shown in Figure 7. The graph shows that the total pressure gradually decreases with the increment in the CFM. Negative values show that the airflow is in a vacuum state. CFD results also show that the CFD results are in good agreement with the experimental measurements with the maximum difference of an average of 1.54%.
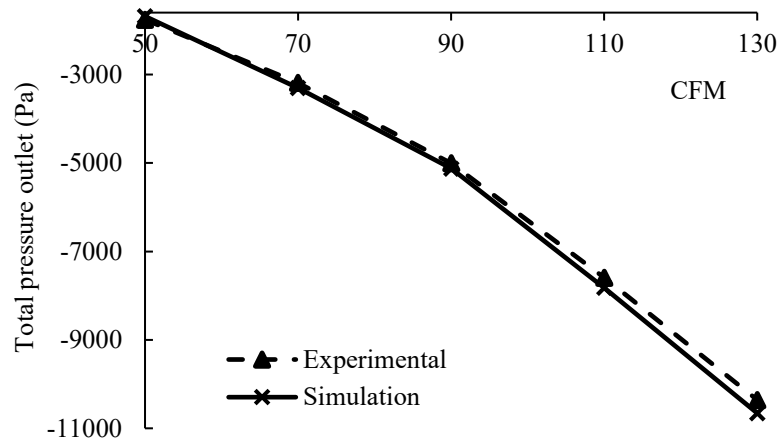
Figure 7. Total pressure outlet against CFM.

Effect of Pressure Drops due to Increasing Mass Flow Rate

Pressure drop across intake system is calculated by taking the difference between an average absolute pressure at the inlet and the outlet of the intake system is shown in Figure 8. As the volumetric airflow rate CFM increase, the pressure drop increases. More air enters the throttle body at wide-open throttle. Notice that the pressure drop difference is very small at low CFM. Figure 9(a) shows the pressure coefficient (C_p) contour on the airbox domain at 90 cfm. The C_p is negative in value towards the suction side of the airbox, while the C_p is positive in the pressure side. The pressure at inlet is almost zero due to near ambient. Low pressure is shown at the exit side of the intake system. It is evident from the contour plots that the pressure inside the domain go through one side only and increases with the exit pressure.
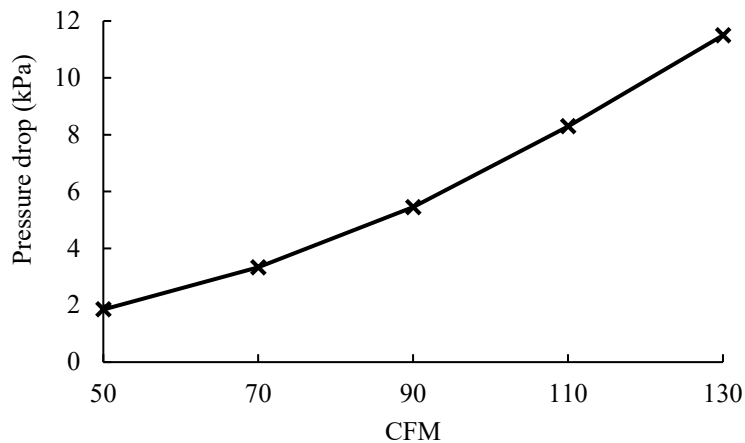

Figure 8. Pressure drops against CFM

The Effect of Skin Friction Coefficient, C_f

Due to the restriction of the space for storing the airbox under the rider seat, this generic airbox is equipped with a snorkel that in S-shaped geometry. The S-shape of the snorkel has a significant effect in flow dynamics and performance of the airbox system as a whole [25]. Figure 9(b) presents the skin friction coefficient, C_f contour of the s-duct at the inlet of the intake system at 90 cfm. The distribution of the C_f contour is the same for all CFM but differs in magnitude. Thus, the C_f contour at 90 cfm is sufficient to show as an example and also in further results. Starting from the inlet of the duct, the $X^* = 0$. Correlating with Figure 9(b), Figure 10(a) shows the C_f at the lower wall of the S-duct inlet started with increasing values during the small converge at the inlet. The C_f then decreases as the flow passage enlarges until at about $X^* = 0.004$. The value increases slowly until $X^* = 0.042$ then continues to increase sharply. This increase is sustained until the sharp bend starts to stabilise, at which the C_f drop sharply.

Near the upper wall of the s-duct in Figure 10(b), the results show a rapid decrease of the C_f in the converging section of the duct. This is followed by a brief increase at the first bend, and a gradual reduction until about $X^* = 0.0355$ due to the surface contact between air particles and the wall is further detached. However, no predicted flow reversal occurs inside this channel. At the second bend, the C_f starts increasing again. All of this behaviour for both walls are reproduced at all tested CFM values. Worth noted, the lower value of CFM, the higher C_f values except for 70 cfm which is the highest.
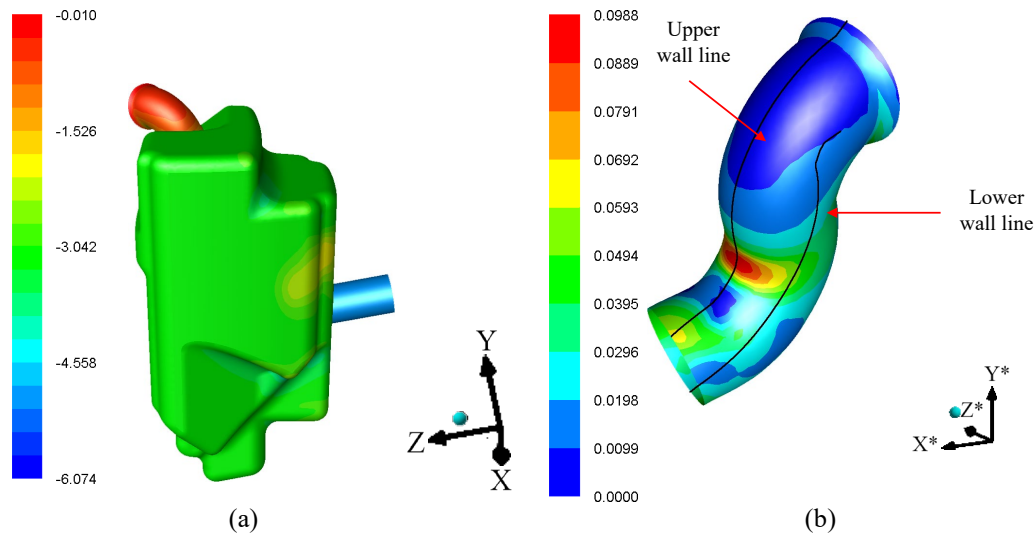
Figure 9. Contour of (a) pressure coefficients and (b) skin friction coefficient on the s-duct inlet at 90 cfm.
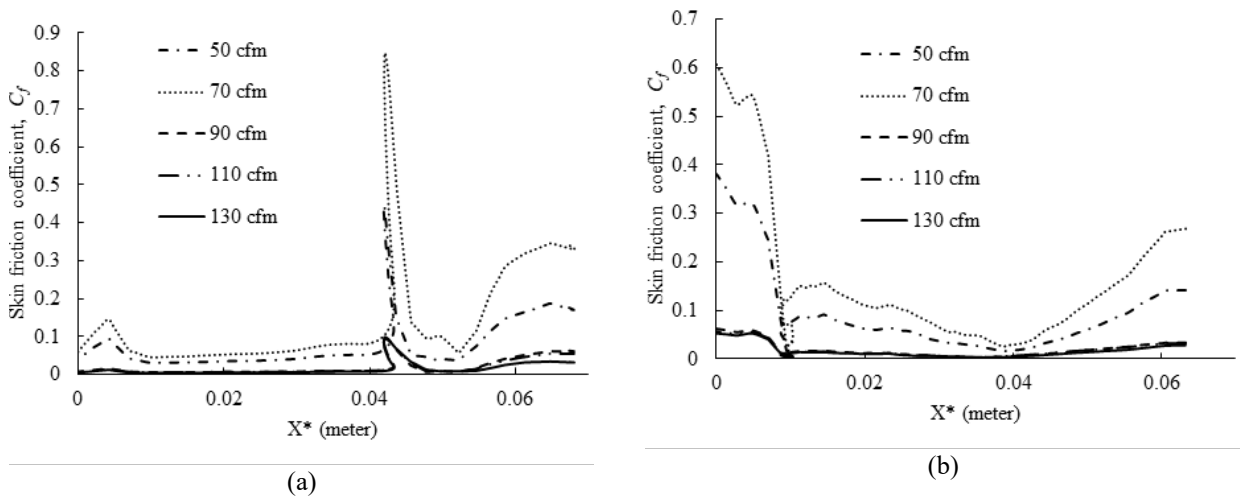

Figure 10. Effects of CFM values on friction coefficients.

Circulation Flow Inside Y15ZR Airbox

Shown in Figure 11 is the path line of air flow in the airbox. The path lines in the plots are tracked from the inlet since there is more air entering the inlet than the outlet. Maximum velocity of 109.09 m/s is observed in the intake system at 90 cfm. Recirculation of flow is seen at edges in the intake system and mainly at the bottom. One thing to notice is that fewer of the streamlines seem to make it through the airbox in the CFD simulation (as tracked from the inlet). Observing from the figure it also possible verify that the maximum flow is going from the inlet exits through the dirty s-duct. Since the outlet of the intake system and the outlet of the inlet pipe is nearer, maximum flow is getting sucked from between this area. One side of the wall was hit, creating high turbulence. This indicates the main role played by the inlet tube in the aerodynamic performance of the airbox. Geometry optimisation can be done to achieve maximum flow rate at the exit flow.

Figure 12 shows the vector plots colourised by the vorticity magnitude of the airflow at 90 cfm within the airbox chamber at section X = 0. The minimum vorticity magnitude at 90 cfm is 21.9 s^{-1} while the maximum is 176,037.45 s^{-1}. The swirl motions within the airbox are obvious with the presence of a few large eddies and hence would lead to enhanced fuel-air mixing. Also, the flow recirculation can be observed at every edge of the chamber. The data obtained also show that the percentage of turbulent intensity in the airbox interior decreases with the increase in CFM (Figure 13). The calculated turbulent intensity shows a steep decrement from 50 cfm to 70 cfm and gradually decreases to 130 cfm as pressure drop increases.
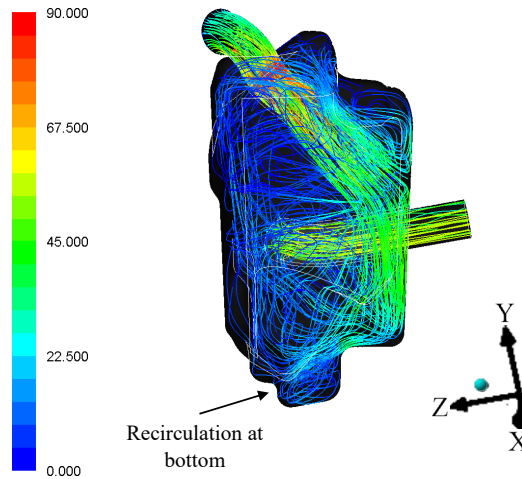
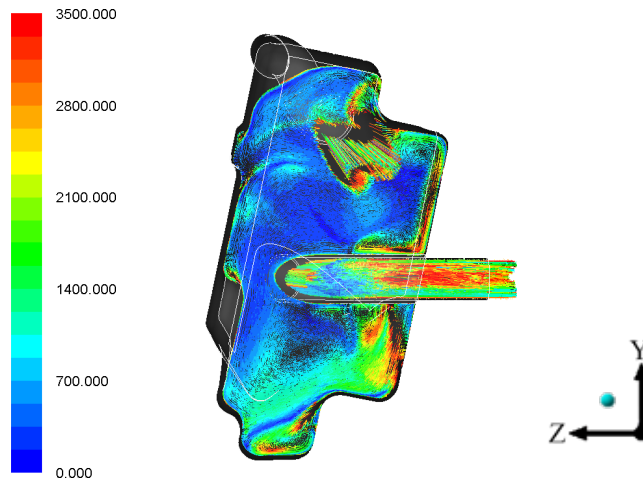**Figure 11.** Path line coloured by velocity magnitude in the airbox at 90 cfm.

Figure 12. Vorticity magnitude vector in the airbox at 90 cfm in section X =0
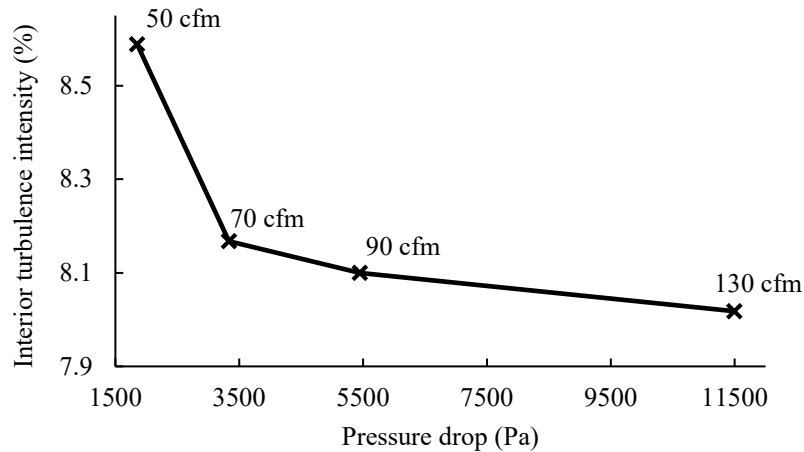

Figure 13. Interior turbulence intensity against pressure drop.

CONCLUSION

Aerodynamic evaluation of a motorcycle airbox was performed as part of a comprehensive computational analysis of the flow from the ambient, through the throttle body and intake port. Flow behaviour through the airbox tube was experimentally and numerically studied. The numerical investigation was conducted using the RANS based ANSYS-Fluent, κ-ω SST turbulence models and validated with an experimental test using the SF-750 flow bench. The mesh with 2.0 million elements is considered throughout this work due to only 1.22% difference with 3 million elements. The SST model turned out to perform with only 1.54% difference in average at the total pressure outlet compared to the experimental tests results. Based on the calculated data, the pressure drops gradually when increasing CFM while the turbulent intensity increases. The high bend angle of the s-duct promoted skin friction. The skin friction coefficient, C_f

on the dirty s-duct at the inlet of the intake system, is higher when the CFM is lower. For the pressure coefficient, C_p on the airbox, it is evident from the contour plots that the pressure inside the domain go through one side only and increases with the exit pressure. Most recirculation of flow is observed at edges in the intake system and mainly at the bottom. The presence of swirl motion and a few large eddies may lead to enhanced fuel-air mixing. For future work, the geometry optimisation can be done to achieve maximum flow rate at the exit flow.

ACKNOWLEDGEMENT

REFERENCES

[1]   Bandyopadhyay D. Airbox for engine. Google Patents, 2017.

[2]   Heywood JB. Internal combustion engine fundamentals: Mcgraw-Hill New York; 1988.

[3]   Salazar F. Internal combustion engines. Department of Aerospace and Mechanical Engineering University of Notre Dame Notre Dame. Retrieved from: https://www.twirpx.com/file/1513521; 11 November 2018.

[4]   Ceviz MA, Akın M. Design of a new SI engine intake manifold with variable length plenum. Energy Conversion and Management. 2010;51(11):2239-2244.

[5]   Singhal A, Parveen M. Air flow optimisation via a venturi type air restrictor. London UK, WCE. 2013.

[6]   Kokkula PR, Bhojappa S, Arslan S, Jawad BA, editors. Design and optimisation of a restrictor of a race car. ASME 2015 International Mechanical Engineering Congress and Exposition; 2015: American Society of Mechanical Engineers.

[7]   Shinde PA. Research and optimisation of intake restrictor for Formula SAE car engine. International Journal of Scientific and Research Publications. 2014;4(4):1.

[8]   Makgata KW. Computational analysis and optimisation of the inlet system of a high-performance rally engine. University of Pretoria; M.Eng Thesis; 2005.

[9]   Pulkrabek W. Engineering fundamentals of the internal combustion engine. Prentice Hall; 2004.

[10]   Das S, Prasad J. Characteristics of a supersonic air-intake with bleed. In: International Conference on Aerospace Science and Technology, Bangalore, India; 26-28 June, 2008.

[11]   Pogorevc P, Kegl B. Optimal design of the intake system. Journal of KONES, 2003; 10(1-2).

[12]   Lee G, Allan W, Boulama KG. Numerical and experimental analysis of the airflow inside an A250 diffuser tube. In: ASME Turbo Expo 2012: Turbine Technical Conference and Expositione, Copenhagen, Denmark, pp. 1703-1712; 2012.

[13]   Taylor GB. Air intake for internal combustion engine. Google Patents, 2002.

[14]   Sulaiman S, Murad S, Ibrahim I, Karim ZA. Study of flow in air-intake system for a single-cylinder go-kart engine. International Journal of Automotive and Mechanical Engineering. 2010;1(1):91-104.

[15]   Giannakopoulos G, Frouzakis C, Boulouchos K, Fischer P, Tomboulides A. Direct numerical simulation of the flow in the intake pipe of an internal combustion engine. International Journal of Heat and Fluid Flow. 2017;68:257-68.

[16]   Rajkumar K, Govindarajan P. Experimental investigation of oxygen enriched air intake on combustion parameters of a single cylinder diesel engine. International journal of engineering science and technology. 2010;2(8):3621-7.

[17]   Bharath P, Kamalakkannan K. Analysis of brake thermal efficiency and oxygen in exhaust using oxygen enriched air in compression ignition engine. IOSR Journal of Mechanical and Civil Engineering (IOSR-JMCE). 2014:PP 30-3.

[18]   Baskar P, Senthilkumar A. Effects of oxygen enriched combustion on pollution and performance characteristics of a diesel engine. Engineering Science and Technology, an International Journal. 2016;19(1):438-43.

[19]   Yerram R, Prasad N, Malathkar PR, Halbe V, Murthy SD. Optimisation of intake system and filter of an automobile using CFD analysis. Quality Engineering & Software Technologies (QUEST), Bangalore, India. 2006.

[20]   Ramasamy D, Zamri M, Mahendran S, Vijayan S, editors. Design optimisation of air intake system (AIS) of 1.6 L engine by adding guide vane. In: International MultiConference of Engineers and Computer Scientists 2010; 2010; Hong Kong.

[21]   HoseopSong BY, Cho H. A study on the optimum shape of automobile air cleaner diffuser. International Journal of Applied Engineering Research. 2017;12(12):3377-81.

[22]   Manikantan R, Gunasekaran EJ. Modeling and analysing of air filter in air intake system in automobile engine. Advances in Mechanical Engineering. 2013;5:654396.

[23]   Phulpagar A, Gohel N. CFD analysis of air intake system. International Journal on Theoretical And Applied Research In Mechanical Engineering. 2015;4(2):45-48.

[24]   Patankar SV, Pratap V, Spalding D. Prediction of turbulent flow in curved pipes. Journal of Fluid Mechanics. 1975;67(3):583-95.

[25]   Halim MA, Mohd NN, Nasir MM, Dahalan M. The evaluation of k-ε and k-ω turbulence models in modelling flows and performance of s-shaped diffuser. International Journal of Automotive and Mechanical Engineering 2018; 15(2):5161-5177.

[26] Sedlacek F, Skovajsa M. Optimization of an Intake System Using CFD Numerical Simulation. Proceedings in Manufacturing Systems. 2016;11(2):71.

[27] Fluent A. Fluent 14.0 User's Guide. ANSYS FLUENT Inc. 2011.

[28] Menter FR. Two-equation Eddy-viscosity turbulence models for engineering applications. AIAA Journal. 1994;32(8):1598-605.

[29] Patankar SV, Spalding DB. A calculation procedure for heat, mass and momentum transfer in three-dimensional parabolic flows. International Journal of Heat And Mass Transfer. 1972;15(10):1787-806.

[30] Van Leer B. Towards the ultimate conservative difference scheme. Journal of Computational Physics. 1997;135(2):229-48.

[31] Tu J, Yeoh GH, Liu C. Computational fluid dynamics: a practical approach: Butterworth-Heinemann; 2012.